J. Condensed Matter Nucl. Sci. 39 (2025) 130–139

Research Article

Refinement Process and Mechanism of Nano Cu-Ni-Zr Alloy by High-Energy Ball Milling

Hui Zhao[1,2], Yan-Xia Liang*[1], Wu-Yun Xiao[1], Wu-Shou Zhang*[2], Da-Hai Liu[1], and Xin-Hua Ma[1]

[1] *State Key Laboratory of NBC protection for Civilian, Beijing 102205, China*
[2] *Institute of Chemistry, CAS, Beijing 100190, China*

Abstract

Nano Cu-Ni-Zr alloys were synthesized using a mixture of Cu, Ni and ZrO_2 powders of 350 meshes through high-energy ball milling for 10 to 50 hours. Analysis via scanning electron microscopy (SEM) and X-ray diffraction (XRD) suggests that the particle nanocrystallization process during ball milling can be divided into four stages: welding, squeezing, fracturing, and dynamic equilibrium. Examination of the particle size distribution and element composition of the Cu-Ni-Zr alloy after 50 hours of milling reveals the formation of a nano-polycrystalline structure with an average grain size of 28 nm. Additionally, this process transforms the initial metal mixture into various alloys such as Ni-Zr, Cu-Ni, as well as compounds like CuO and ZrO_2. Calorimetry using this alloy in low-energy-nuclear-reaction experiments exhibited excess heat.
 ISSN 2227-3123

Keywords: High-energy ball milling, Nanocrystal, Cu-Ni-Zr Alloy, Microstructure, Refinement mechanism

1. Introduction

Nickel alloys, as traditional alloy materials, have undergone extensive development over the years. Recently, there has been a notable focus on new functional alloy materials with good heat-resistance, leading to increased interest in their comprehensive nuclear and thermal properties [1]–[3]. These alloys primarily include nickel-copper (Ni-Cu) series, nickel-zirconium (Ni-Zr) series and nickel-chromium (Ni-Cr) series. Of particular interest is the Cu-Ni-Zr alloy, which stands out for its high strength, elevated temperature resistance, corrosion resistance, and excellent fatigue properties among other characteristics. Consequently, this alloy finds widespread application in high-speed rail transportation, electronic communication, anti-irradiation materials, lead frame materials, rocket-engine combustion chamber and other fields [4]. In addition, the hydrogen absorption properties of Cu-Ni-Zr alloys have attracted attention for potential use in low-energy nuclear reactions (LENR) and catalytic applications [5]–[7]. To further enhance the properties of Cu-

*Corresponding authors. E-mail: yxliang0701@126.com; wszhang@iccas.ac.cn.

 ISSN 2227-3123

Ni-Zr alloys, solid solution strengthening and precipitation strengthening have proven effective methods; additionally alloying and nanocrystallization are essential requirements [8], [9].

High-energy ball milling (HEBM) is one of the methods that can be used to prepare ultrafine alloy materials [10], [11]. When compared to the wet chemical method, the nanocrystalline Cu-Ni-Zr alloy prepared by HEBM has been found to be more practical and effective [12]. Furthermore, HEBM has demonstrated utility in the synthesis of stable and metastable phases of various alloy materials, including intermediate, solid solution and amorphous alloy phases. For instance, Liu et al. prepared and studied Cu-Zr alloy materials by mechanical-ball milling method, revealing that that part of Zr could be solid-dissolved into Cu to form a Cu-Zr supersaturated solid solution, and the other part formed Cu-Zr intermetallic compounds [13]. Shang et al. conducted experiments on Cu-Nb and Cu-Mo alloys using HEBM, and analyzed the factors influencing the experimental results such as the ball-to-powder ratio and ball diameter distribution [14]. Additionally, Panek and Karolus employed the same method to prepare Ti-Cu alloy, studying the structural evolution of the alloy during milling and heat treatment, as well as the formation of nano solid solutions [15].

Ball milling has the capacity to manufacture nanoparticles and different alloy phase materials. Most of the current research focuses on the two-phase structure, as the addition of one phase leads to a great increase in the complexity of the internal structure of the material. However, complex material systems are crucial for the development of functional materials. Therefore, it is imperative to carry out relevant research. Furthermore, current studies mainly examine the grain refinement and alloying of materials post-HEBM from a microstructure perspective, while the characteristic transformation of powder materials during HEBM is rarely reported. Specifically, the complete process and intrinsic mechanism of grain refinement caused by HEBM require more attention.

In this study, Cu-Ni-Zr alloy powder with an average particle size of 28 nm was prepared by adjusting the critical parameters of HEBM, and the optimal preparation conditions were given. At the same time, this research also aims to characterize and analyze the microstructure of samples after different milling time by scanning electron microscopy (SEM) and X-ray diffraction (XRD), so as to study and elucidate the grinding process, evolution process and formation mechanism of nanoparticles in different stages of HEBM. The experimental parameters of nanocrystalline Cu-Ni-Zr alloy powder prepared by HEBM were optimized, and the key factors controlling the ball milling process were discussed, which provided guidance and strategy for the design and controllable preparation of advanced LENR alloy functional materials.

2. Experimental Set-up

To prepare the nano Cu-Ni-Zr alloy, the initial Ni, Cu and ZrO_2 (all from ZhongYan Precise Instrument (Beijing) Technology Co., Ltd) powders with a purity of 99.9% and an average particle size of 350 mesh were used. FRITSCH P-7 planetary ball mill was used at room temperature. The ball mill operates at a speed of 500 rpm, with a transmission ratio between the revolution and spin of the tanks set as 1:2. In order to minimize the temperature influence on the samples, an intermittent grinding mode was adopted. The tanks and balls (ϕ5 mm) used in the milling process were made of tungsten carbide (WC), and pre-grinding was carried out before milling to ensure that the surface of the grinding ball was covered with the corresponding powder material and reduce the contamination from impurities. The weight ratio of ball to powder was set at 10:1, as measured using a Mettler Toledo ME204T balance. The chromatography-grade ethanol (Aladdin Scientific Corp.) with a purity better than 99.997% was used as the process control agent (PCA) to reduce wall adhesion and improve grinding efficiency. The grinding tank was filled with N_2 gas (purity 99.999%) from the beginning.

The samples acquired through HEBM at various milling durations were analyzed using SEM with X-ray energy dispersion spectrometry (EDS, FEI Nano 430) and XRD (Panak Sharpening series). Particle size statistics were conducted using Nanomeasure software. The SEM image was magnified using the software until the edges of the samples

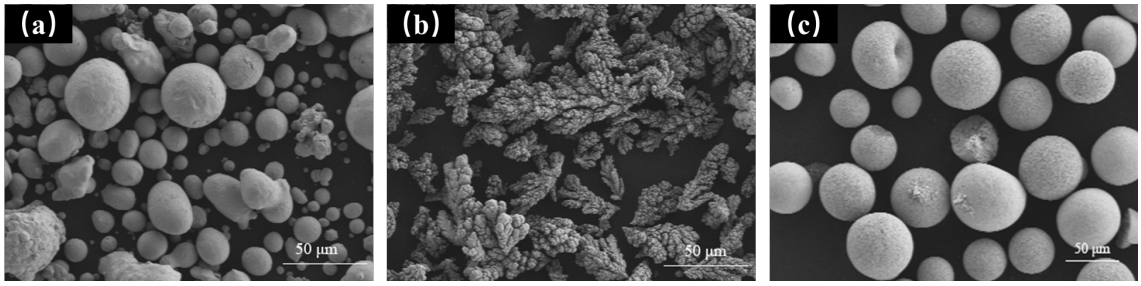

Figure 1. SEM images of initial Cu (a), Ni (b) and ZrO_2 (c) powders.

were clearly distinguishable. The Martin diameter, which refers to the length of the area bisecting line of the polygon particle in the horizontal measurement direction, was used to define the particle size. Over 200 particles were counted in each image, and a statistical graph depicting particle size distribution was generated through mapping.

3. Results and Discussion

The initial powder materials used in this study underwent basic characterization prior to ball milling. This preliminary analysis was crucial for gathering relevant data for comparative purpose. Figure 1 shows the SEM images of the Cu, Ni and ZrO_2 powders, which exhibit a simple polycrystalline structure as confirmed by XRD. Cu and ZrO_2 particles are spherical, whereas the Ni particles display a dendritic morphology. The maximum particle size for all materials is approximately 50 μm.

3.1. Preparation and Analysis of Cu-Ni-Zr Powder

Based on the recipe of materials in LENR (with an atomic ratio Cu:Ni:Zr = 1:7:14 [16]), the initial Cu, Ni and ZrO_2 powders were weighed according to their respective masses. The HEBL process was carried out using the aforementioned ball mill for a total duration of 50 hours. Prior to this, pre-ball milling was performed with powder of the same composition to clean the miller. Subsequently, SEM and related test were applied to the resulting material. Figure 2 shows the SEM and EDS of Cu-Ni-Zr (i.e., CNZ, strictly speaking, it is the mixture of binary alloys and oxides) samples after 50 hours of ball milling (i.e., CNZ-50). It can be seen that CNZ-50 samples exhibit granular morphology with significant agglomeration because of the high surface energy of the samples after HEBM. However, this adhesion and agglomeration are very weak so that the powder could be uniformly dispersed by placing it in the solution. Figure 2(b) shows a high-resolution SEM image of the dispersed CNZ-50, which has nearly spherical shape. The diameters of two particles, as marked in Fig. 2(b), are 27 and 38 nm, respectively. A thorough analysis of particles' size distribution was conducted on the powder sample and the statistical graph is shown in Fig. 2(c). The particle sizes range from 9 to 97 nm, with 97% of particle measuring below 50 nm and Consequently, the average particle size is 28 nm.

Figure 2(d) and (e) show the distribution of element content and image of backscattered SEM of CNZ-50, where a specific shape of closed dashed curve in specific individual color represents a specific particle. It can be seen that a large number of Cu, Ni, Zr and O elements were detected in the sample measured by EDS, with a relatively uniform distribution of all elements. The red-dashed curve region indicates the presence of Cu-Ni alloy particles, with low levels of Zr and O, and high levels and evenly distributed Ni and Cu, suggesting local Cu-Ni alloys. In the yellow-dashed curve region, the distribution of O is even, but that of Ni, Cu and Zr exhibit an opposite distribution, indicating a multi-

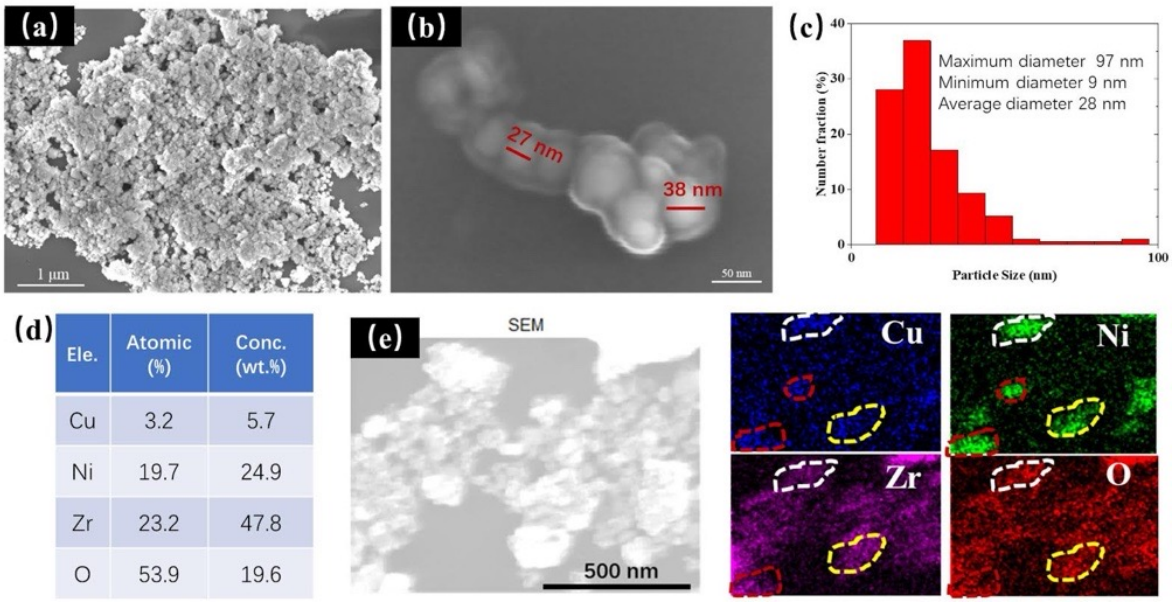

Ele.	Atomic (%)	Conc. (wt.%)
Cu	3.2	5.7
Ni	19.7	24.9
Zr	23.2	47.8
O	53.9	19.6

Figure 2. Characteristics of CNZ-50. (a) and (b) SEM images of different magnitudes, (c) Statistical histograms of grain size. (d) The content table of the corresponding regions. (e) The backscattered SEM image and the element distribution map, in which the dashed curves of different colors enclose the different regions of the sample particles.

grain with different elements. However, due to resolution limitations, obtaining more detailed elemental distribution seems not feasible. The white-dashed curve region shows a more uniform distribution of the four elements in the particles, indicating that Cu, Ni and ZrO_x were well mixed here. Based on the EDS analysis, the Cu, Ni and Zr ratio was about 1:6.2:7.7, differing from the initial ratio. This disparity may be attributed to the limited acquisition area and the semi-quantitative nature of EDS, which can result in significant detection deviation for ZrO_x.

Given the limitations of SEM microstructure characterization, obtaining comprehensive macroscopic information about samples appears to be infeasible. Consequently, conducting XRD analysis is essential for examining the macroscopic phase structure of the samples. Figure 3 presents the XRD pattern of the CNZ-50, with peak positions labeled by the software. Compared with the initial powder, there are more peaks with varying values of full-width half maximum (FWHM) in the XRD pattern of the sample after ball milling. Specifically, the peaks marked with blue circles correspond to ZrO_2, the peaks indicated by green triangles represent the Ni-Zr alloy, while those marked with black stars denote the Cu-Ni alloy. Additionally, a peak labeled with a red circle corresponds to CuO. There are numerous peaks of ZrO_2 with narrow FWHMs, which is due to the high content of ZrO_2 in the initial powder, with parts of it remaining unalloyed in the process. Nonetheless, the particle size of ZrO_2 has been significantly reduced. Moreover, new components such as Ni-Zr, Cu-Ni and CuO, which were not present in the initial powders are observed after processing. These facts demonstrate the effectiveness of HEBM as an alloying method. Furthermore, in the sample after ball milling, the initial metals of Cu and Ni disappeared, being replaced by the alloys, which could be attributed to the binding energy between the metal bonds favoring the formation of intermetallic compounds. Moreover, the broad FHWMs and low peak positions of the formed Ni-Zr and Cu-Ni phases suggest small grain sizes and higher density of phase defects in the alloys. During the milling process, some Zr forms alloys with Ni and Cu, while a small amount of free oxygen combines with other metals. Due to the influence of nickel oxidation mechanism and ZrO_2 particles

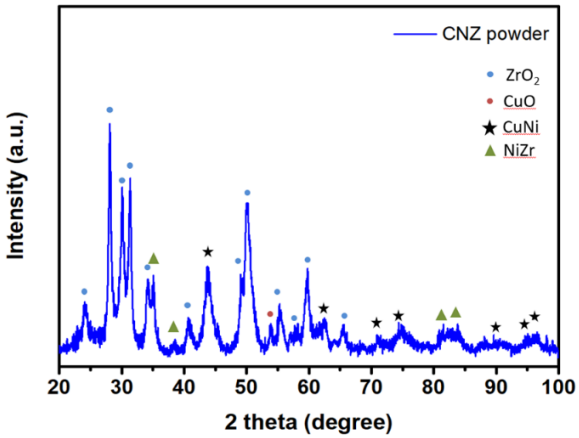

Figure 3. The XRD pattern of CNZ-50.

present in the system [17], [18], CuO is observed in XRD pattern; however, NiO was not detected, as illustrated in Fig. 3.

By carefully selecting the appropriate parameters of ball milling, it is possible to reduce the initial powder particle size from 45 μm down to 28 nm, which is a significant achievement in CNZ alloys. HEBM has also proven effective for alloying different metals. Consequently, it is crucial to understand the influence of the ball milling process on the microstructure of powder particles. Experimental studies can elucidate the relationship between ball milling parameters and sample structure, providing valuable insights that can be used to develop effective guidelines and strategies for targeted nanomaterial preparation.

3.2. Effect of Milling Time on Microstructure Evolution of CNZ Powder

The experimental conditions were the same as those in Section 2. Samples were taken from the tanks in the vacuum glove box after effective milling intervals of 10, 20, 30, 40 and 50 h, being labeled CNZ-10, CNZ-20, CNZ-30, CNZ-40 and CNZ-50, respectively. These samples were then subjected to characterizations to evaluate the effect of the milling process on the microstructure.

Figure 4 shows CNZ powder samples prepared by ball milling from 10 to 50 hours. Figure 4(a) is a SEM image and statistical histograms of grain sizes of CNZ-10. At this stage, the sample exhibits a sheet structure and the welded structures of sintering necks are visible between the particles. It can be seen that the sample size has decreased from the micron to the nanometer scale after HEBM for 10 h. The statistical distribution presents a unimodal distribution with the maximum particle size of 229 nm and the minimum of 21 nm. The distribution width is substantial, with 73% of particles falling within the size range of 20 to 100 nm and the remaining 27% exceeding 100 nm. Figure 4(b) illustrates the characteristics of CNZ-20. The SEM image reveals the uniform distribution and flake polygon structure of the samples. The stacking and welding structure observed in earlier stages almost disappears, indicating significant changes in the particle morphology. The flake particles have grown in size, with the largest one now measuring 436 nm. Additionally, small particles are attached to the surface of larger ones, with sizes ranging between 20 and 150 nm. The average grain size of the entire sample is 106 nm.

As the milling time progresses, the size of the flake structure gradually increases, and smaller particles begin to emerge. Due to the extrusion effect, these particles undergo axially compression and radial stretching, resulting in large

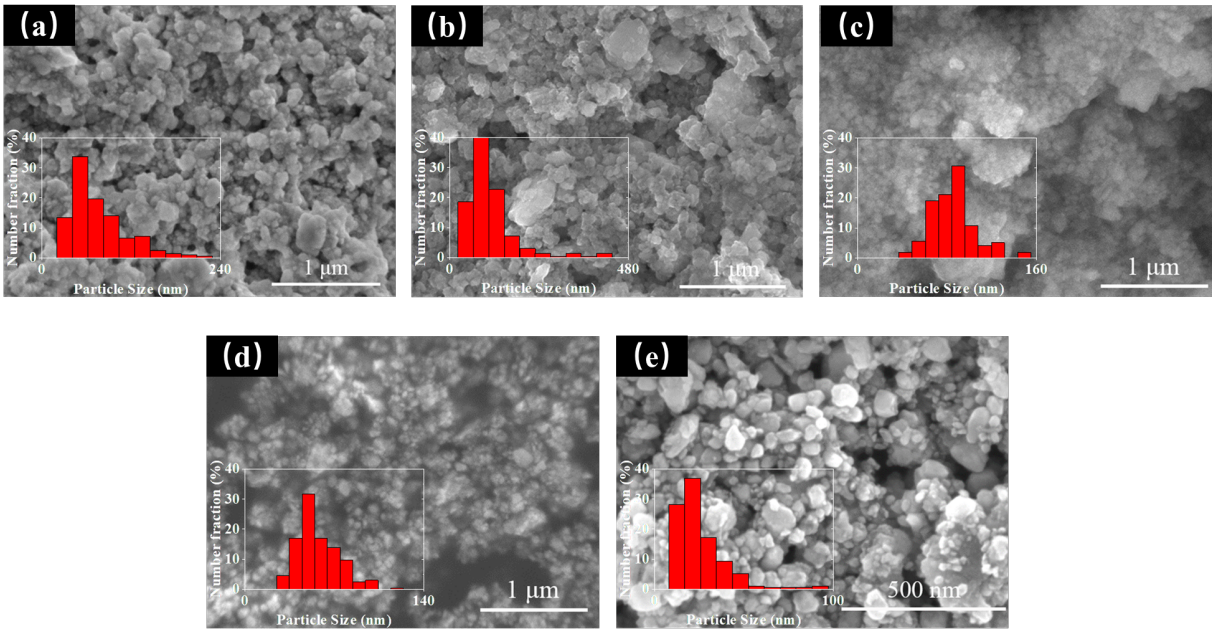

Figure 4. SEM images and statistical histograms of grain sizes of (a) CNZ-10, (b) CNZ-20, (c) CNZ-30, (d) CNZ-40, and (e) CNZ-50.

and thin CNZ nano-sheets. Concurrently, shear and friction forces cause particles to peel off from the surface, making it rougher than before. At this stage, as energy accumulation intensifies, the diffusion mechanism of CNZ is enhanced, leading to an almost complete disappearance of the welded structure. Over time, the layered particles continue to grow thinner until small particles reappear.

Figs. 4(c) and (d) show SEM images and alongside statistical histograms of grain sizes of CNZ-30 and CNZ-40, respectively. These images illustrate the progression of the particle morphology and dispersion characteristics throughout the milling process. During this phase, the lamellar structure progressively diminishes while the number of small particles increases.

The high-resolution SEM image in Fig. 4(b) reveals the presence of numerous small particles resulting from fragmentation. Statistical analysis shows that the minimum particle size in the sample is 37 nm, with the maximum particle size reduced from 435 nm in the previous stage to 155 nm. After milling for 40 hours, the dispersion of the sample improves further. The SEM image in Fig. 4(c) illustrates uniformly dispersed particles, with sizes ranging from 25 to 124 nm. Notably, particles smaller than 100 nm constitute 96% of the total population. Additionally, during this milling stage, the statistical distribution of sample sizes increasingly approximates a Gaussian distribution, suggesting that an equilibrium state of fragmentation is being approached.

After extending the ball milling process to 50 hours, the powder refining continues without significant changes. At this stage, all CNZ powders have transformed from micron-sized particles to nanoparticles (< 100 nm), with an average particle size of 28 nm. In subsequent stages of the process, these smaller particles exhibit high surface activity, leading to agglomeration. As milling time increases, both particle separation and agglomeration occur simultaneously. Based

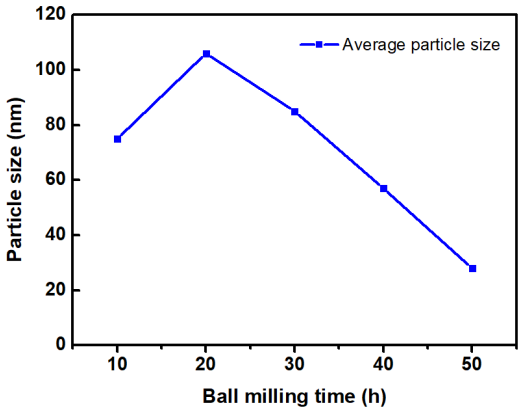

Figure 5. The average particle size of CNZ sample varies with milling time.

on energy balance conditions, the relationship between critical stress and particle size can be expressed as follows [19]:

$$\sigma = \sqrt{\frac{3\pi E\sqrt{i}}{4\left(1-v^2\right)D}} \tag{1}$$

where σ is shear stress; E and v are Young's elastic modulus and Poisson's ratio, respectively; i is the surface free energy and D is the particle diameter. From this formula, it is evident that as particle size decreases, shear stress will increase significantly. When the particle size reaches the nanoscale, the corresponding critical shear stress reaches up to megapascals. Beyond this point, the required shear stress to further reduce particle size becomes so high that it exceeds the capacity of the milling system. Consequently, despite extended milling time, there will be no further reduction in particle size; instead, the CNZ's particle size stabilizes and reaches an equilibrium [20].

To elucidate the changes occurring throughout the milling process over time, the relationship between the average particle size of CNZ sample and the milling duration was analyzed as shown in Fig. 5. The analysis indicates that during nanocrystallization, particle size does not decrease monotonically with increased milling time. Instead, it initially increases before subsequently decreasing. Examination of the microstructure reveals that this pattern corresponds to the influence mechanism of HEBM on powder particles. Our 50-hour experiment encompasses four distinct stages of ball milling. Based on our experience [20], extending the ball milling duration would eventually lead to a dynamic equilibrium stage. However, since a 50-hour period meets the requirements for LENR experiments, further experiment was deemed unnecessary and thus not conducted.

3.3. Changes in the Distribution of Element in CNZ Powder

To investigate the influence of ball milling process on the element distribution in CNZ, SEM-EDS analysis was conducted using a sample of CNZ-10 as shown in Fig. 6. The results reveal that after 10 hours of ball milling, elemental mixing has commenced within the sample. Among the four elements analyzed, Zr exhibits both the highest content and most uniform distribution. Ni and Cu are embedded within the Zr matrix, while O tends to be distributed more prominently on particle surfaces. These observations indicate that atomic migration behavior is already occurring at this stage of the ball milling.

After 10 hours of HEBM, the morphology of the CNZ sample transforms from a polygonal to a sheet-like structure, with powder particles becoming welded together. This morphological change is primarily attributed to the impact force

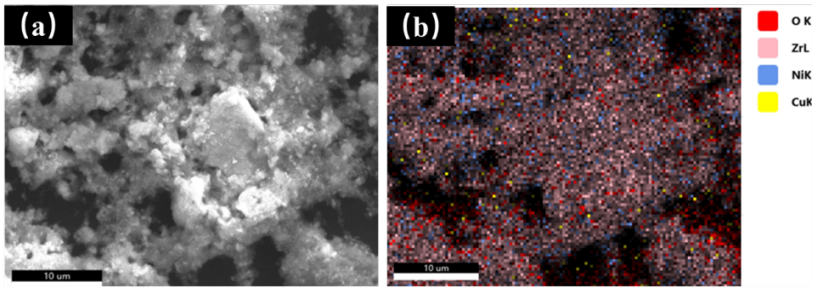

Ele.	Conc. (wt.%)	Atomic (%)
Cu K	2.9	1.6
Ni K	17.8	10.4
Zr L	46.5	17.5
O K	32.8	70.5

Figure 6. (a) Backscattered SEM image, (b) element distribution and (c) and element content table of CNZ-10.

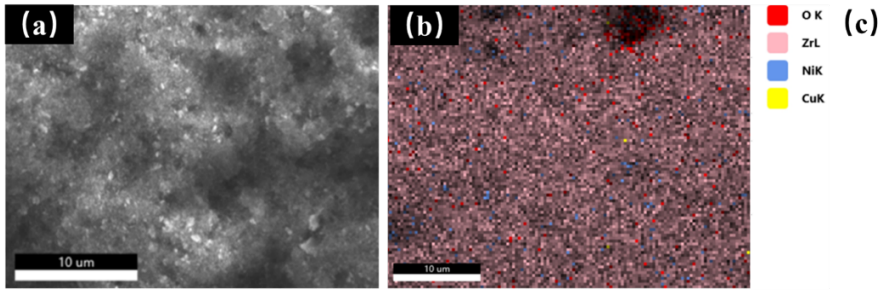

Ele.	Conc. (wt.%)	Atomic (%)
Cu K	2.6	1.4
Ni K	15.6	9.1
Zr L	48.8	18.4
O K	33.0	71.1

Figure 7. (a) Backscattered SEM image, (b) element distribution and (c) element content table of CNZ-40.

exerted by the grinding ball and tank on the stacked powder particles. The applied force increases the internal energy of these particles, facilitating the migration and mixing of metal atoms. Consequently, the CNZ powder particles adopt a flatter morphology, and welded structures emerge. However, at this stage, the powder particles do not acquire sufficient energy for complete mixing; welding occurs only between overlapping particles.

Figure 7 shows the backscattered SEM image of the CNZ-40 sample along with its corresponding element distribution mapping. In comparison to the CNZ-10 samples, the CNZ-40 sample exhibits a more uniform distribution of Zr, Ni, Cu and O elements. Notably, the O element has penetrated into the interior of the powder material, indicating a more comprehensive atomic migration process due to extended milling time. This progression towards a more homogeneous element distribution suggests deeper atomic migration and thorough metal evolution.

At this stage, the morphology of CNZ samples transitions from flake to fragment, with a marked reduction in particle size as grinding time increases. Beyond the extrusion effect, shear and friction during the ball milling process significantly impact the sample's characteristics. Shear forces and frictional impacts on the flaky particles induce stress concentration and subsequent cracking, which crushes them into smaller fragments. By 40 hours of milling, sufficient energy has accumulated for the sample to fully enter the fracturing stage; all flaky particles become thinner and are reduced to small particles. This process also promotes atomic migration within the sample, resulting in a more uniform distribution of its elements.

The milling process can be divided into several stages. The initial stage involves welding, during which particles entering the ball mill tank stack on top of each other and become welded together under the impact force of the grinding balls, gradually forming a sheet-like structure. As milling continues and energy input persists, the radial structure of these welded particles enlarges while their axial structure thins due to ongoing impact and friction forces, leading to

an increase in particle size. With further milling time, shear friction becomes predominant, causing small fragments to detach from the flake structure and form smaller particles. This results in a reduction in the size of the flake-structured particles. However, as milling time extended further, a critical shear stress is reached. At this point, an equilibrium state is achieved where crushing and bonding processes balance out for nano-sized CNZ particles, making additional particle size reduction increasingly difficult [20].

4. Conclusion

This study offers a comprehensive analysis of the morphological characteristics and microstructure evolution of Cu-Ni-Zr powder materials during high-energy ball milling. The impact and shear effects exerted by the grinding balls on the material were identified as key factors influencing both the nano-processing and alloying process of Cu-Ni-Zr powder.

Building on these experiments and previous research [20], we propose a model for the refining process and mechanism of Cu-Ni-Zr alloy, which comprises four stages: welding, squeezing, fracturing, and dynamic equilibrium. In the welding stage, Cu-Ni-Zr particles overlap and fuse together under impact forces, resulting in flake-like powder shapes. During the squeezing stage, these lamellar particles become thinner as energy accumulates. The fracturing stage involves breaking down particles into small fragments with size less than 100 nm. Finally, with increased milling time, a dynamic balance is achieved where fracture and re-connection of Cu-Ni-Zr fragments reach a stable equilibrium state. By optimizing the technical parameters for high-energy ball milling, we successfully prepared nanometer-sized Cu-Ni-Zr powder particles smaller than 30 nm; the smallest observed particle size was 9 nm.

Additionally, it is noteworthy that calorimetry using this alloy in LENR experiments exhibited excess heat. Further work is required to confirm the heat, so detailed results will be published later.

References

[1] Y. Iwamura, T. Itoh, J. Kasagi, A. Kitamura, A. Takahashi, K. Takahashi and R. Seto, Replication experiments at Tohoku university on anomalous heat generation using nickel-based binary nanocomposites and hydrogen isotope gas. *J. Condensed Matter Nucl. Sci.* **24** (2017) 191–201.

[2] A. Kitamura, A. Takahashi, K. Takahashi, R. Seto, Y. Matsuda, Y. Iwamura, T. Itoh, J. Kasagi, M. Nakamura, M. Uchimura, H. Takahashi, T. Hioki, T. Motohiro, Y. Furuyama, M. Kishida and H. Matsune, Collaborative examination on anomalous heat effect using nickel-based binary nanocomposites supported by zirconia. *J. Condensed Matter Nucl. Sci.* **24** (2017) 202–213.

[3] L. B. Ber, S. V. Rogozhkin, A. A. Khomich and A. G. Zaluzhnyi, Distribution of alloying element atoms between γ- and γ'-phase particles in a heat-resistant nickel alloy. *Phys. Met. Metall.* **123** (2022) 163–177.

[4] T. Kulikova, A. Maiorova, V. Bykov and K. Shunyaev, Chemical interaction and thermodynamic properties of (Cu,Ni)-Zr glass-forming alloys. *Eur. Phys. J-Spec. Top.* **226** (2017) 1097–1106.

[5] Y. Iwamura, T. Itoh, J. Kasagi, A. Kitamura, A. Takahashi, K. Takahashi, R. Seto, M. Uchimura, H. Takahashi, T. Hioki, T. Motohiro, Y. Furuyama, M. Kishida and H. Matsune, Anomalous heat effects induced by metal nano-composites and hydrogen gas. *J. Condensed Matter Nucl. Sci.* **29** (2019) 119–128.

[6] A. Takahashi, H. Ido, A. Hattori, R. Seto, A. Kamei, J. Hachisuka, T. Yokose, Y. Mori, A. Taniike and Y. Furuyama. Latest progress in research on AHE and circumstantial nuclear evidence by interaction of nano-metal and H(D)-gas. *J. Condensed Matter Nucl. Sci*. **33** (2020) 14–32.

[7] G. X. Pei, X. Y. Liu, X. F. Yang, L. L. Zhang, A. Q. Wang, L. Li, H. Wang, X. D. Wang and T. Zhang, Performance of Cu-alloyed Pd single-atom catalyst for semihydrogenation of acetylene under simulated front-end conditions. *ACS Catal.* **7** (2017) 1491–1500.

[8] I. Altenberger, H. A. Kuhn, H. R. Müller, M. Mhaede, M. Gholami-Kermanshahi and L. Wagner, Material properties of high-strength beryllium-free copper alloys. *Int. J. Mater. Prod. Tec.* **50** (2015) 124 –146.

[9] K. L. Lv, Z. Y. Xie, H. S. Liu, G. M. Cai and Z. P. Jin, Experimental investigation of phase equilibria in the Cu–Ni–Zr system. *J. Mater. Sci.* **50** (2015) 7238–7247.

[10] F. L. Zhang, C. Y. Wang and M. Zhu, Nanostructured WC/Co composite powder prepared by high energy ball milling. *Scripta Mater.* **49** (2003) 1123–1128.
[11] H. G. Tang, X. F. Ma, W. Zhao, X. W. Yan and R. J. Hong, Preparation of W–Al alloys by mechanical alloying. *J. Alloys Compd.* **347** (2002) 228–230.
[12] M. Xia, Q. Z. Yan, L. Xu, H. Y. Guo, L. X. Zhu and C. C. Ge, Bulk tungsten with uniformly dispersed La_2O_3 nanoparticles sintered from co-precipitated La_2O_3/W nanoparticles. *J. Nucl. Mater.* **434** (2013) 85–89.
[13] D. W. Liu, Y. C. Wu, D. B. Wang, X. M. Huang and Y. C. Zhen, Characteristics and pressing-sintering process of Cu-Zr powder formed by high-energy ball milling. *J. Hefei Univ. Tech. (Natural Science)* **32** (2009) 1711–1715.
[14] X. K. Shang, X. T. Wang and S. L. Chen, Effects of ball milling processing conditions and alloy components on the synthesis of Cu-Nb and Cu-Mo alloys. *Materials* **12** (2019) 1224 (9 pages).
[15] J. Panek and M. Karolus, Structural studies on Ti–Cu alloy obtained by high-energy ball milling. *Mater. Sci. Tech.* **36** (2020) 978–981.
[16] A. Kitamura, A. Takahashi, K. Takahashi, R. Seto, T. Hatano,Y. Iwamura, T. Itoh, J. Kasagi, M. Nakamura, M. Uchimura, H. Takahashi, S. Sumitomo, T. Hioki, T. Motohiro, Y. Furuyama, M. Kishida and H. Matsune, Excess heat evolution from nanocomposite samples under exposure to hydrogen isotope gases. *Int. J. Hydrogen Energy* **43** (2018) 16187–16200.
[17] J. S. Choi, S. H. Sin and K. Y. Lee, The oxidation of specpure nickel. *J. Korean Chem. Soc.* **10** (1966) 153–157.
[18] Y. B. Du, L. Q. Zhu, C. H. Liu and Z. Q. Bai, High temperature oxidation resistance of composite nickel plating layer containing SiO_2 and ZrO_2 particles. *J. Beijing Univ. Aero. Astro.* **10** (2004) 1003–1007.
[19] J. Sun, Z. J. Deng, Z. H. Li and M. J. Tu, Fracture strength of spheroidal carbide particle. *Int. J. Fracture* **42** (1990) 39–42.
[20] Y. X. Liang, Z. M. Wu, E. G. Fu, J. L. Du, P. P. Wang, Y. B. Zhao, Y. H. Qiu and Z. Y. Hu, Refinement process and mechanisms of tungsten powder by high energy ball milling. *Int. J. Refract. Met. Hard Mater.* **67** (2017) 1–8.